G133.50+9.01: A likely cloud-cloud collision complex triggering the formation of filaments, cores and a stellar cluster

Namitha Issac[1]★, Anandmayee Tej[1]†, Tie Liu[2,3], Yuefang Wu[4]
[1]Indian Institute of Space Science and Technology, Thiruvananthapuram 695 547, Kerala, India
[2]Shanghai Astronomical Observatory, Chinese Academy of Sciences, 80 Nandan Road, Shanghai 200030, People's Republic of China
[3]Key Laboratory for Research in Galaxies and Cosmology, Chinese Academy of Sciences, 80 Nandan Road, Shanghai 200030, People's Republic of China
[4]Department of Astronomy, Peking University, 100871, Beijing, China

arXiv:2009.13731v1 [astro-ph.SR] 29 Sep 2020

Accepted XXX. Received YYY; in original form ZZZ

ABSTRACT

We present compelling observational evidence of G133.50+9.01 being a bona fide cloud-cloud collision candidate with signatures of induced filament, core, and cluster formation. The CO molecular line observations reveal that the G133.50+9.01 complex is made of two colliding molecular clouds with systemic velocities, −16.9 km s^{-1} and −14.1 km s^{-1}. The intersection of the clouds is characterised by broad bridging features characteristic of collision. The morphology of the shocked layer at the interaction front resembles an arc like structure with enhanced excitation temperature and H_2 column density. A complex network of filaments is detected in the SCUBA 850 μm image with 14 embedded dense cores, all well correlated spatially with the shocked layer. A stellar cluster revealed through an over-density of identified Class I and II young stellar objects is found located along the arc in the intersection region corroborating with a likely collision induced origin.

Key words: ISM: clouds – ISM: kinematics and dynamics – ISM: individual objects (G133.50+9.01) – radio lines: ISM – stars: formation

1 INTRODUCTION

There is growing evidence that cloud-cloud collision can trigger star and cluster formation (Torii et al. 2015; Gong et al. 2017; Sano et al. 2018; Liu et al. 2018a,b). Hydrodynamic simulations (Habe & Ohta 1992; Anathpindika 2010; Takahira et al. 2014) reveal that collisionally compressed interfaces form dense, self-gravitating cores. Magneto-hydrodynamic (MHD) simulations by Inoue & Fukui (2013) and other recent studies (e.g. Wu et al. 2015; Fukui et al. 2016; Li et al. 2018; Torii et al. 2017; Ohama et al. 2018; Gong et al. 2019; Tokuda et al. 2019; Sano et al. 2019) give insightful discussions indicating the importance of cloud-cloud collision in high-mass star and cluster formation. The proposed picture involves supersonic collisions that boost the magnetic field strength and gas density in the shock-compressed layer. This results in an enhanced mass accretion rate and also a large effective Jeans mass, the two prime ingredients for massive star formation. The shocked layer collapses into a filament with an enhanced self-gravity in the post-shock gas. A number of pre-stellar cores, accreting mass from the natal cloud are formed in these filaments. Recent studies on a dark cloud L1158 by Gong et al. (2017, 2019) show evidence of collision triggered cluster formation of low- and intermediate-mass stars as well. Notwithstanding the complexities involved in deciphering cloud kinematics from stellar feedback, observationally, many cloud-cloud collision candidates have been discovered (see Hayashi et al. 2020, and references therein). If cloud collision is frequent in disk galaxies like Milky Way (Tasker & Tan 2009), then detailed investigation of cloud-cloud collision candidates can shed crucial light on triggered star formation under different physical conditions. A recent paper by Fukui et al. (2020) provides an excellent review on the current status of observations and theoretical understanding of cloud-cloud collisions and also discusses future directions in this area.

In this paper, we investigate the Planck Galactic Cold Clump (PGCC), G133.50+9.01, using molecular line observation. Located in the field of the classical Cepheid SU Cas, a young cluster associated with G133.50+9.01 is identified by Majaess et al. (2012) using 2MASS and WISE photometry. The cluster that contains countless young stellar objects (YSOs) deviates from spherical symmetry and exhibits an apparent diameter of 3×6 arcmin. Zhang et al. (2018) detected 18 dust cores from the 850 μm map. We present new results on this complex based on a comprehensive analysis of the CO line kinematics and morphology in conjunction with infrared and sub-mm data to understand the related stellar population and dust component.

2 OBSERVATIONS

2.1 PMO observations

The ^{12}CO (1 – 0) and ^{13}CO (1 – 0) lines were observed with the Purple Mountain Observatory 13.7-m telescope (PMO-13.7 m) in August 2013, as a part of PMO survey of Planck Galactic Cold Clumps (Wu et al. 2012; Liu et al. 2012; Zhang et al. 2018). The nine beam array receiver system in single-sideband mode was used as the

★ E-mail: namithaissac.16@res.iist.ac.in (NI)
† E-mail: tej@iist.ac.in (AT)

© 2020 The Authors

front end (Shan et al. 2012). The half-power beam width (HPBW) is 56 arcsec and the main-beam efficiency is ∼ 0.45. ^{12}CO (1 − 0) and ^{13}CO (1 − 0) lines were obtained simultaneously. FFTS spectrometers were used as back ends, which have a total bandwidth of 1 GHz and 16384 channels, corresponding to a velocity resolution of 0.16 km s^{-1} for the ^{12}CO (1−0) and 0.17 km s^{-1} for the ^{13}CO (1−0). The on-the-fly (OTF) observing mode was utilized. The scan speed is 20 arcsec s^{-1} and the mapping area is 22 arcmin × 22 arcmin. These data are smoothed with a beam size of ∼ 63 arcsec. The typical rms noise level per channel is 0.3 K in T_A^* for the ^{12}CO (1 − 0) and 0.2 K for the ^{13}CO (1 − 0).

2.2 SCUBA 850 μm data

The dust continuum observation at 850 μm was carried out in November 2014 using Submillimeter Common-User Bolometer Array 2 (SCUBA-2, Holland et al. 2013) on the James Clerk Maxwell Telescope (JCMT). JCMT is a 15-m telescope single-dish telescope that operates in the submillimetre wavelength region of the spectrum. This instrument can provide an effective beam size of 14.6 arcsec in the 850 μm band. The "CV Daisy" mapping mode was used with a mapping area of about 12 arcsec × 12 arcsec. The data are reduced using SMURF in the STARLINK package. The rms level is around 18.1 mJy beam^{-1}.

2.3 Dust polarization data from Planck

To determine the orientation of the magnetic field in the region associated with G133.50+9.01, we make use of the *Planck* 353 GHz (850 μm) dust continuum polarization data (Planck Collaboration et al. 2016a). The polarization data including the Stokes *I*, *Q* and *U* maps used are from the *Planck* Public Data Release 2 Full Mission Map with PCCS2 Catalog[1] (Planck Collaboration et al. 2016b). These maps have a beam size of ∼ 5 arcmin and a pixel size of ∼ 1 arcmin.

2.4 WISE archival data

To identify the stellar population associated with G133.50+9.01, we use the mid-infrared (MIR) archival data from Wide-field Infrared Survey Explorer (WISE, Wright et al. 2010). WISE mapped the sky at the MIR wavelengths 3.4, 4.6, 12, and 22 μm with angular resolutions of 6.1, 6.4, 6.5, and 12.0 arcsec, respectively. We retrieve sources from the ALLWISE[2] catalog using NASA/IPAC Infrared Science Archive (IRSA). ALLWISE combines the data from the WISE cryogenic and NEOWISE (Mainzer et al. 2011) post-cryogenic survey phases. Combining the two data products, ALLWISE provides enhanced photometric sensitivity and accuracy, and better astrometric precision.

3 RESULTS

3.1 Distance to G133.50+9.01

Citing the nature of CO and HI emission, Majaess et al. (2012) speculate that the cluster may coincide with the complex in the foreground of SU Cas (which is at a distance of 418 ± 12 pc) or, beyond it at a distance, $d \leq 950$ pc. In their study, Zhang et al. (2018) use the Bayesian distance estimation method proposed by Reid et al. (2016). Here, trigonometric parallaxes from the Bar and Spiral Structure Legacy Survey and Japanese VLBI Exploration of Radio Astrometry are combined with the probability density function (PDF) for kinematic distance, displacement from the plane, and proximity to individual parallax sources to generate a combined PDF. Taking the observed centroid velocity of the ^{13}CO (1 − 0) line, Zhang et al. (2018) estimate the distance to G133.50+9.01 to be 0.61 ± 0.14 kpc. In this paper, we implement an alternate approach to estimate the distance following the method outlined in Gong et al. (2017). This procedure makes use of the 3D dust reddening map[3] from Green et al. (2019). The dust reddening maps presented by these authors are based on 2MASS and Pan-STARRS 1 photometric data in combination with GAIA parallaxes. The distance to estimated by measuring the cumulative reddening, $E(B-V)$, along the line-of-sight. Four sightlines, marked by crosses in Fig. 2(b), are selected. The median cumulative reddening towards these four sightlines are plotted as a function of the distance in Fig. 1. The reddening plot towards the sightlines 1 and 3 overlap. The plot shows a steep rise in $E(B-V)$ at a distance of ∼ 840 pc. Such a steep rise can be attributed to the dust reddening in G133.50+9.01. $E(B-V)$ towards the sightline 4 shows an additional steep rise at a distance of ∼ 4.2 kpc. This possibly indicates the presence of a background, unrelated cloud. In the analysis presented in this paper, we have taken 840 pc as the distance to G133.50+9.01.

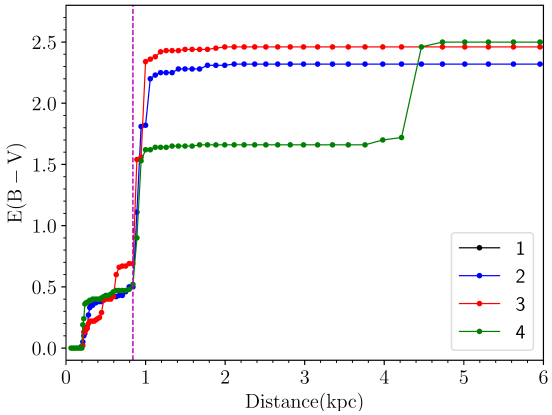


Figure 1. The cumulative reddening along four sightlines marked by crosses in Fig. 2(b). The reddening plot towards sightline 1 overlaps with that towards sightline 3. The dashed vertical line indicates the estimated distance to G133.50+9.01.

3.2 CO morphology of G133.50+9.01 complex

Morphology of the G133.50+9.01 complex is deciphered using molecular line observations of CO. The ^{12}CO (1 − 0) emission is usually considered to be optically thick throughout the molecular cloud, and hence an excellent tracer of its spatial extent, rather than the density distribution. The ^{13}CO (1 − 0) emission, on the other hand, is less optically thick and probes the denser regions of the molecular cloud. The integrated intensity maps of ^{12}CO (1 − 0) and ^{13}CO (1 − 0) line emission towards G133.50+9.01 in three velocity ranges are shown in Fig. 2(a)-(c). Similar morphology is displayed

[1] https://irsa.ipac.caltech.edu/applications/planck/
[2] http://wise2.ipac.caltech.edu/docs/release/allwise/
[3] http://argonaut.skymaps.info

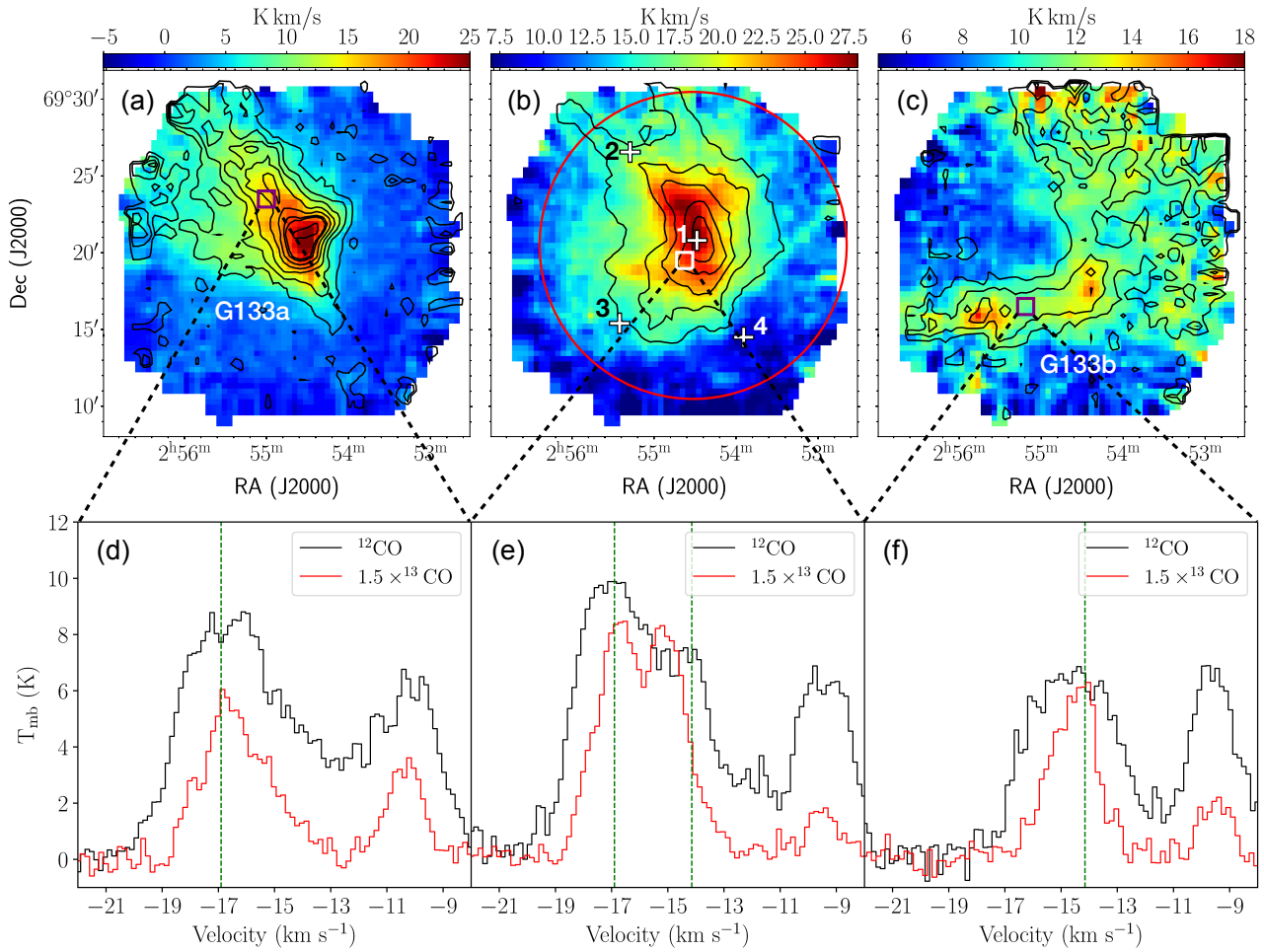


Figure 2. (a) The colour scale depicts the ^{12}CO (1 – 0) integrated intensity within the velocity −19.4 to −16.9 km s^{-1}. The contours of the ^{13}CO (1 – 0) emission over the same velocity range is overlaid in black with levels starting from 3σ and increasing in steps of 3σ (σ = 0.5 K km s^{-1}). (b) Same as (a) with the integration velocity range −16.9 to −14.1 km s^{-1}. The ^{13}CO (1 – 0) contours start from 3σ and increases in steps of 2σ (σ = 1.0 K km s^{-1}). The white crosses mark the regions towards which the median cumulative reddening is estimated to find the distance. The red circle describes a region of radius 10 arcmin over which the young stellar population is identified (Section 3.6). (c) Same as (a) with the integration velocity range −14.1 to −11.6 km s^{-1}. The ^{13}CO (1 – 0) contours start from 3σ and increases in steps of 2σ (σ = 0.6 K km s^{-1}). (d)-(f) The ^{12}CO (1 – 0) (black) and ^{13}CO (1 – 0) (red) spectra extracted at three different positions of the cloud complex G133.50+9.01, indicated by squares in (a)-(c). The vertical green lines indicate the systemic velocities of G133a and G133b as estimated from the ^{13}CO (1 – 0) line

in both emission lines. The molecular cloud has an elongated morphology in the north-east direction in the velocity range −19.4 to −16.9 km s^{-1} as is evident from Fig. 2(a), an arc like morphology in the velocity range −16.9 to −14.1 km s^{-1}, shown in Fig. 2(b). In the range −14.1 to −11.6 km s^{-1}, a hemispherical, 'boomerang-like' morphology with a cavity opening towards the north-east and extended emission towards the north-west is noticeable in Fig. 2(c). The emission morphology seen in the above velocity ranges suggests the likely presence of two coalescing molecular clouds (hereafter G133a and G133b) associated with G133.50+9.01. The ^{12}CO (1 – 0) and ^{13}CO (1 – 0) spectra extracted, sampling these clouds and the intersection region is plotted in Fig. 2(d)-(f). The spectra corresponding to G133a and G133b have single peaked line profiles. From the peak of the ^{13}CO (1 – 0) line, the systemic velocities of G133a and G133b are estimated to be −16.9 km s^{-1} and −14.1 km s^{-1}, respectively. The intersection region clearly shows two velocity components. From the spectra of the interaction region presented, it is seen that for cloud G133b, the peak velocity of the ^{13}CO (1 – 0) line is offset from the estimated systemic velocity of −14.1 km s^{-1}. This can be attributed to the interaction of the colliding clouds resulting in an intermediate velocity in the intersection region.

Fig. 2(d)-(f) show an additional velocity component at ∼ −10 km s^{-1} in all three spectra presented. To understand this, we construct channel maps of ^{12}CO (1 – 0) and ^{13}CO (1 – 0) emission in the velocity range −19.0 to −7.0 km s^{-1}. These are plotted in Fig. 3. As can be seen from the maps, emission from G133a and G133b peaks in the velocity range −18.0 to −16.0 km s^{-1} and −15.0 to −13.0 km s^{-1}, respectively. An arc like morphology, as seen in Fig. 2(b) is evident at intermediate velocities. In the channel maps for the velocity range, −12.0 to −9.0 km s^{-1}, another component is visible which is consistent with the spectra in Fig. 2(d)-(f). As discussed in Section 3.1, the reddening plot along the sightline covering this component (# 4) shows two steep rises at distances 0.84 kpc and 4.2 kpc. Given that the velocity is ∼ −10 km s^{-1}, this cloud is likely to be at a similar distance as that of G133a and G133b with a background, unassociated cloud farther away.

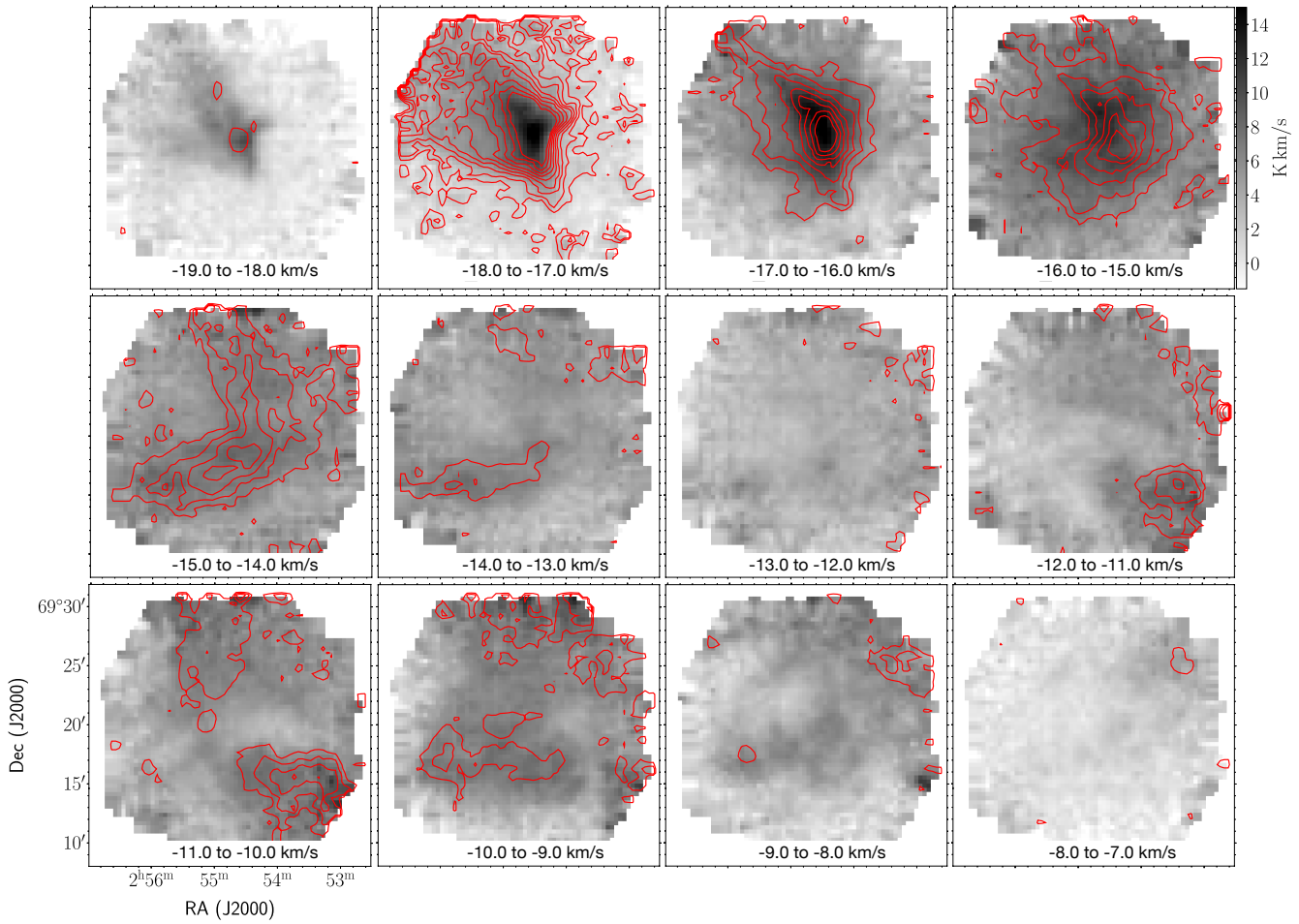


Figure 3. Chanel maps for region associated with G133.50+9.01. The grey scale shows the ^{12}CO (1 – 0) channel map. Each map has a channel width of 1 km s^{-1}. The contours of the ^{13}CO (1 – 0) emission at each velocity channel is overlaid in red. The contours start at 3σ (σ = 0.5 K km s^{-1}) and increases in steps of 2σ.

Under the assumption of local thermodynamic equilibrium, the total mass of the molecular clouds can be estimated from the optically thin ^{13}CO emission. Following Szűcs et al. (2016), the column density of ^{13}CO is calculated and from the abundance ratio of ^{13}CO to H_2, the H_2 column density is estimated. To determine the ^{13}CO column density, the effective line-of-sight excitation temperature is determined. Combining the radiative transfer equation and the Rayleigh-Jeans law, the brightness temperature can be expressed as,

$$T_{\rm mb} = T_0 \left(\frac{1}{e^{T_0/T_{\rm ex}} - 1} - \frac{1}{e^{T_0/T_{\rm bg}} - 1} \right) (1 - e^{-\tau}) \quad (1)$$

Here $T_0 = h\nu/k_{\rm B}$, h is the Planck's constant, $k_{\rm B}$ is the Boltzmann's constant, $T_{\rm bg}$ = 2.7 K is the background temperature, and τ is the optical depth. Assuming that the ^{12}CO (1 – 0) emission is optically thick ($\tau \gg 1$), the excitation temperature per pixel of ^{12}CO (1 – 0) spectral cube is given by

$$T_{\rm ex} = 5.5 \ln \left(1 + \frac{5.5}{T^{12}_{\rm mb,peak} + c_1} \right)^{-1} \quad (2)$$

where, $T^{12}_{\rm mb,peak}$ is the peak intensity of ^{12}CO (1 – 0) at each pixel, 5.5 K = $h\nu(^{12}{\rm CO})/k_{\rm B}$, and constant c_1 = 0.82 for $T_{\rm bg}$ = 2.7 K. From the ^{12}CO (1 – 0) spectral cube, the $T^{12}_{\rm mb,peak}$ map is built, from which, using Equation 2, the excitation temperature map of ^{12}CO (1 – 0) is constructed which is shown in Fig. 4(a). We assume that the excitation temperatures of ^{12}CO (1 – 0) and ^{13}CO (1 – 0) are equal along the line-of-sight. Substituting for $T_{\rm ex}$ and the ^{13}CO (1–0) peak brightness temperature in Equation 1, the pixel-wise optical depth can be derived following the equation,

$$\tau_{13} = -\ln \left[1 - \frac{T^{13}_{\rm mb,peak}}{5.3} \left\{ \left(e^{5.3/T_{\rm ex}} - 1 \right)^{-1} - c_2 \right\}^{-1} \right] \quad (3)$$

where, $T^{13}_{\rm mb,peak}$ is the peak brightness temperature of ^{13}CO (1 – 0), 5.3 K = $h\nu(^{13}{\rm CO})/k_{\rm B}$, and c_2 = 0.16. Assuming that the excitation temperature equals the kinetic temperature for all the energy states and the levels are populated according to Boltzmann distribution, the ^{13}CO column density is calculated from the optical depth using the following expression

$$N(^{13}{\rm CO}) = 3.0 \times 10^{14} \times \frac{\tau_{13}}{1 - e^{-\tau_{13}}} \times \frac{\int T^{13}_{\rm mb}(v) dv}{1 - e^{-5.3/T_{\rm ex}}} \quad (4)$$

$\int T^{13}_{\rm mb}(v) dv$ is the integrated intensity over velocity in units of km s^{-1}.

Fig. 4(b) shows the H_2 column density map constructed with a constant [^{12}CO/^{13}CO] isotopic ratio of 77 (Wilson & Rood 1994) and a [$H_2/^{12}$CO] abundance ratio of 1.1×10^4 (Frerking et al. 1982).

Considering the region within the 3σ level of the ^{13}CO (1 – 0) emission integrated over the velocity range −19.4 to −11.6 km s^{-1}, the mean line-of-sight H_2 column density, $N(H_2)$, is calculated to be 8.7×10^{21} cm^{-2}. Subsequently, the total mass of the molecular cloud complex (= $N(H_2)\mu_{H_2} m_H A$; A is the physical area of the cloud complex, m_H is the mass of hydrogen atom) is estimated to be 2.6×10^3 $M_\odot$. Here, the mean molecular weight, μ_{H_2} is taken to be 2.8. The individual masses of G133a and G133b are computed to be $1.1{\times}10^3$ $M_\odot$ and $1.4{\times}10^3$ $M_\odot$, respectively, with the assumption that both clouds have equal contribution to the mass at the intersection.

Fig. 4(a) shows the ^{12}CO (1 – 0) excitation temperature map overlaid with the contours of ^{13}CO (1 – 0) emission integrated over the velocity range −16.9 to −14.1 km s^{-1}. The intersection of the clouds, G133a and G133b reveals an open arc structure. The ^{13}CO emission also follows a similar arc like morphology. The radius of curvature of the arc is ∼ 1.6 pc. The excitation temperatures within this arc varies from 13 – 20 K and is higher than that of the ambient cloud (∼ 11 K). The H_2 column density map given in Fig. 4(b) also reveals a density enhancement along this arc.

3.3 Cloud kinematics

The ^{12}CO (1 – 0) and ^{13}CO (1 – 0) position-velocity (PV) diagram of the G133.50+9.01 complex is constructed to understand its velocity structure. Fig. 5(a) depicts the two-colour composite integrated intensity map of ^{12}CO (1 – 0) integrated between −19.4 to −16.9 km s^{-1} (blue) and −14.1 to −11.6 km s^{-1}(red). The 3σ contours of the integrated ^{13}CO (1 – 0) within the same velocity ranges is overlaid. PV slices are extracted along two directions, A and B, highlighted in Fig. 5(a). These slices probe G133a and G133b, respectively. Both, ^{12}CO (1 – 0) and ^{13}CO (1 – 0) emission show intermediate "bridging features" between the peak velocities, −16.9 and −14.1 km s^{-1} highlighted by black arrows in Fig. 5(b), (c) and (e). Apart from these, in Fig. 5(b) and (c), high-velocity ^{12}CO wings are also evident.

3.4 Dust filaments and cores

Fig. 6 shows the 850 μm dust emission towards G133.50+9.01. A visual inspection of the 850 μm map reveals that the emission from the dust component has a filamentary structure in the north-south direction that bifurcates at the ends. The skeletons of the filaments are overlaid on the image. Localized dust peaks are seen along the filaments. We use the FellWalker clump identification algorithm (Berry 2015), which is part of the Starlink CUPID package, to identify the dust cores in this region. A detection threshold of 2.5σ (σ = 18.1 mJy beam^{-1}) is used and pixels outside the 2.5σ level are considered noise. Using this method we detect 14 dust cores along the filaments that are named according to their positions in the field. Relative to the central core, C1, four cores, N1-N4, extend towards the north and five cores, S1-S5, extend towards the south along one of the filaments. The remaining four cores, NE1 and SE1-SE3 lie along the other filaments in the north-east and south-east directions, respectively. The retrieved apertures of these cores are superimposed on the 850 μm map shown in Fig. 6. Correlation with Fig. 4(b) shows that the detected cores are located within the arc structure displaying enhanced column density. The mass of each core is estimated from the total 850 μm flux density integrated within the core aperture. Assuming thermal emission from optically thin dust, the following expression is used,

Table 1. Physical parameters of the identified dust cores associated with G133.50+9.01.

Dust Core	Peak position		Radius	Mass
	α(J2000) (^{h} ^{m} ^{s})	δ(J2000) ($^\circ$ $'$ $''$)	(pc)	($M_\odot$)
C1	2 54 30.33	69 20 39.80	0.20	86.0
N1	2 54 34.11	69 21 51.80	0.12	27.9
N2	2 54 31.84	69 23 39.80	0.09	10.8
N3	2 54 31.84	69 24 15.80	0.06	2.8
N4	2 54 35.63	69 24 43.80	0.07	2.5
NE1	2 54 43.21	69 23 19.78	0.08	9.5
S1	2 54 25.80	69 19 47.79	0.14	34.6
S2	2 54 17.49	69 19 27.76	0.06	5.2
S3	2 54 25.05	69 18 43.79	0.09	8.6
S4	2 54 30.34	69 17 47.80	0.05	2.5
S5	2 54 24.31	69 17 23.79	0.05	2.6
SE1	2 54 37.89	69 19 15.80	0.12	13.3
SE2	2 54 47.70	69 19 15.76	0.05	2.0
SE3	2 54 46.94	69 18 27.76	0.07	3.7

$$M_C = \frac{S_\nu d^2}{\kappa_\nu B_\nu(T_d)} \tag{5}$$

Here, S_ν is the flux density at 850 μm, d is the distance, T_d is the dust temperature of the cores taken to be the mean excitation temperature, 15.3 K, within the open arc structure, and $\kappa_\nu = 0.1(\nu/1200\,\mathrm{GHz})^\beta$ is the dust opacity. β, the dust emissivity index, is assumed to be 2. The effective radii, $r = (A/\pi)^{0.5}$, of the dust cores are determined from the area, A, enclosed within the retrieved apertures. Peak positions, radii and masses of the dust cores are tabulated in Table 1.

3.5 Magnetic field orientation

Planck polarization data is used to determine the magnetic field orientation in the vicinity of G133.50+9.01. Following the IAU convention, the linear polarization angle (PA) is given by, $\psi_{IAU} = 0.5 \times arctan(-U/Q)$ in the Galactic coordinate system (Planck Collaboration et al. 2015). The plane of sky orientation of the magnetic field is obtained by adding 90° to the PA ($\chi' = \psi_{IAU} + 90°$). The position angle of the magnetic field in the equatorial coordinate system, FK5, is then estimated following the discussion in Corradi et al. (1998), where

$$\psi = arctan\left[\frac{cos\,(l - 32.9°)}{cos\,b\,cot\,62.9° - sin\,b\,sin\,(l - 32.9°)}\right] \tag{6}$$

Here, ψ is the angle subtended by the directions of the equatorial north and the Galactic north at each pixel of the *Planck* polarization maps. The orientation of the magnetic field at each pixel with Galactic coordinates, l and b is then transformed from the Galactic coordinate system (χ') to the equatorial system (χ) using the relation,

$$\chi = \chi' - \psi \tag{7}$$

The mean magnetic field orientation is determined by taking the average of the χ values that lie within the 3σ level of the ^{13}CO (1 – 0) emission over the velocity range −19.4 to −11.6 km s^{-1}. The

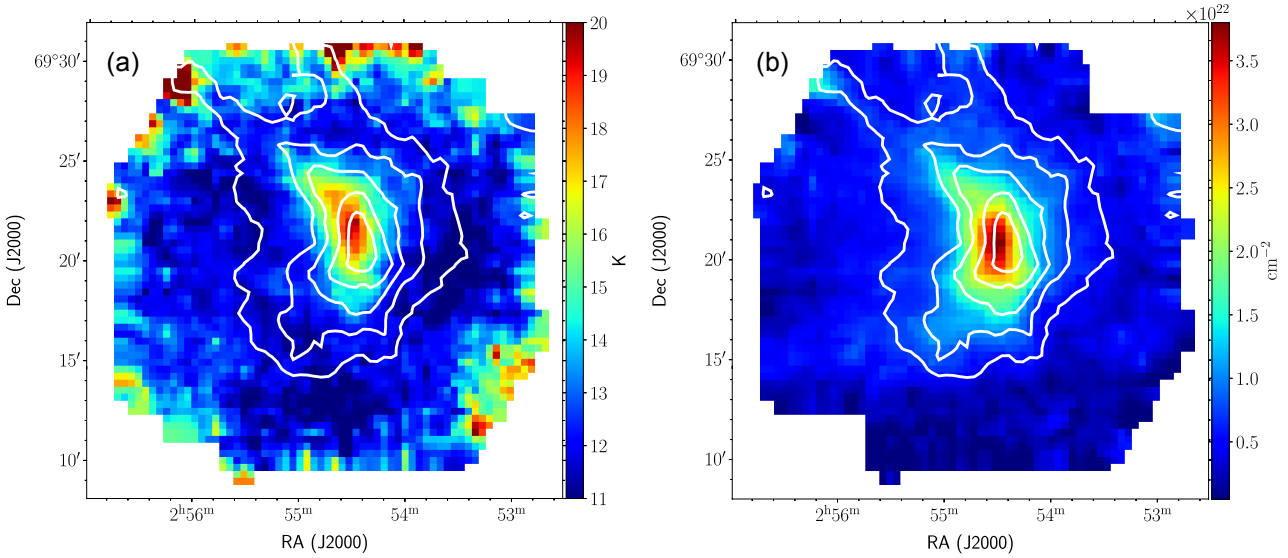


Figure 4. (a) The excitation temperature map of G133.50+9.01 derived from the peak intensity of the ^{12}CO (1 – 0) emission. (b) The H_2 column density map of the region associated with G133.50+9.01 constructed following the steps described in Section 3.2. The white contours correspond to the ^{13}CO (1 – 0) emission within the velocity range −16.9 to −14.1 km s^{-1}. The contour levels are same as in Fig. 2(b).

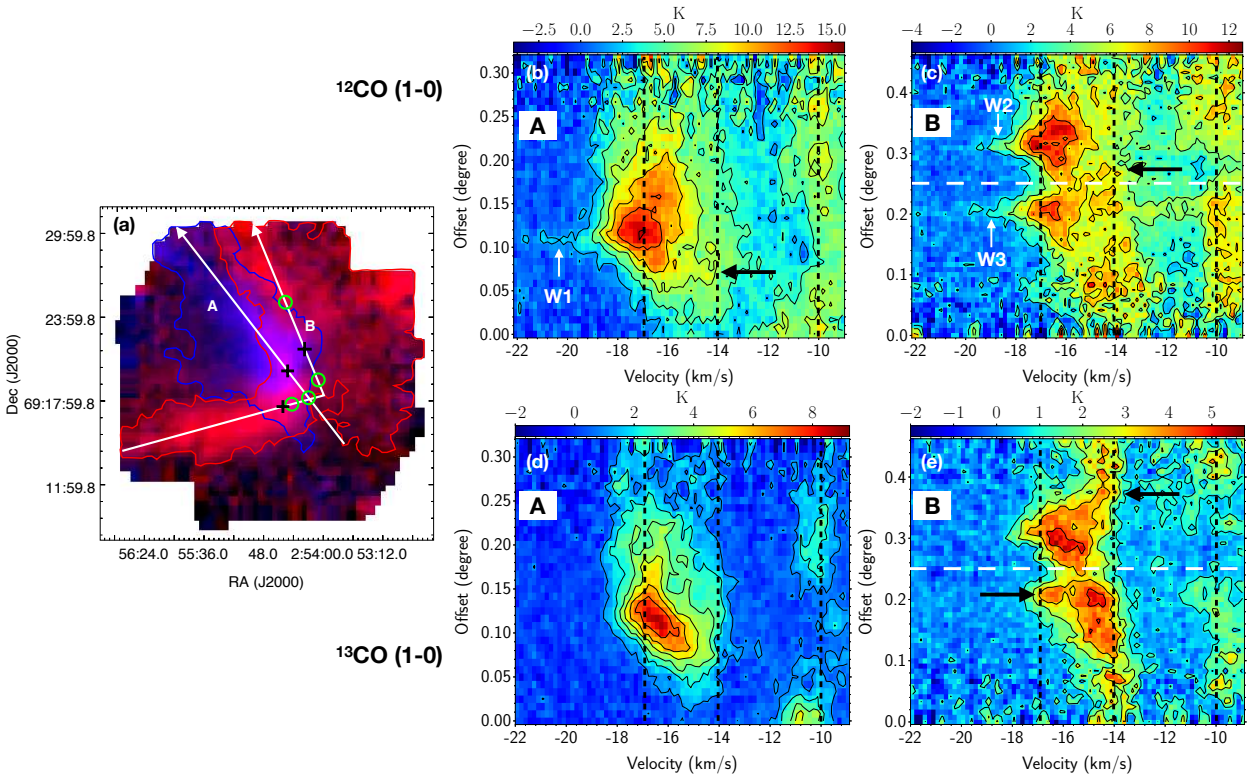


Figure 5. (a) Two-colour composite integrate intensity map of ^{12}CO (1 – 0) integrated between −19.4 to −16.9 km s^{-1} (blue) and −14.1 to −11.6 km s^{-1} (red) of the G133.50+9.01 complex. The 3σ contour of the ^{13}CO (1 – 0) emission (same as in Fig. 2a and c) at both velocity ranges is overlaid in blue and red. A and B are the cuts along which the PV slices are extracted, sampling G133a and G133b, respectively. (b) and (d) PV diagram of ^{12}CO and ^{13}CO, respectively along the cut A. (c) and (e) Same as (b) and (d) along the cut B. The horizontal dashed line delineates the PV slices on either side of the bend in B. The contours start at 3σ and increases in steps of 4σ (σ = 0.6 K for ^{12}CO and 0.3 K for ^{13}CO). The vertical dashed lines represent the systemic velocities of G133a, G133b and the cloud at ∼ −10 km s^{-1}. The bridging features with intermediate velocity are marked by black arrows. The positions of the bridging features on the PV cut is marked by green circles in (a). The ^{12}CO wings are indicated by white arrows and their positions on the PV cut are indicated by black crosses in (a).

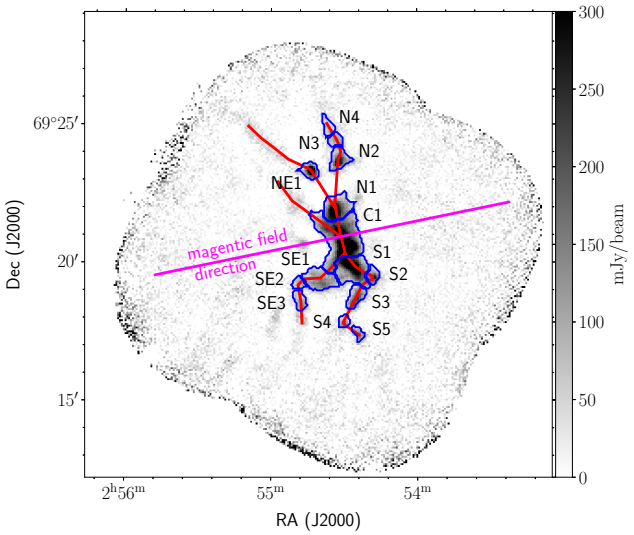


Figure 6. The dust emission at 850 μm in the region surrounding G133.50+9.01 is presented here. The FellWalker retrieved apertures of the dust cores are outlined in blue and are labelled according to their positions in the field. The skeletons of the visually identified filaments are sketched in red. The magenta line represents the orientation of the magnetic field with respect to the filaments.

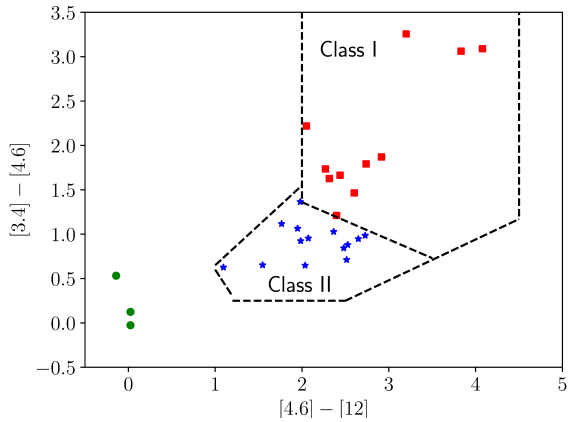


Figure 7. WISE color-color diagram for the bands, 3.4, 4.6 and 12 μm used to identify and classify YSOs associated with G133.50+9.01. The dashed lines denotes the criteria used by Koenig & Leisawitz (2014) to delineate the YSO classes. Green circles denote the sources that do not satisfy the YSO criteria.

orientation is estimated to be 99.1 ± 5.6° east of north and is traced in Fig. 6 with respect to the filaments identified from the 850 μm map.

3.6 Associated young stellar population

Using 2MASS-K_s and WISE photometry data, Majaess et al. (2012) have discovered a crowded cluster of 53 YSOs associated with G133.50+9.01. We revisit the cluster detection and YSO identification by considering a larger (radius of 10 arcmin) region, centred at 02:54:31.4 +69:20:32.5, which effectively samples the entire G133.50+9.01 cloud complex. The circular region over which the YSOs are identified is sketched in Fig. 2b and Fig. 9. For YSO identification, we implement the colour classification scheme of Koenig & Leisawitz (2014) using the improved ALLWISE catalogue (Cutri & et al. 2013). After removal of fake or spurious sources and extragalactic contaminants, a WISE colour-colour diagram is constructed and shown in Fig. 7. Using the colour criteria set by Koenig & Leisawitz (2014), we identify 11 (39%) Class I and 14 (50%) Class II sources in our field. Sources not satisfying the prescribed criteria could be either Class III/weak disk YSOs, blue transition disk objects, or AGB stars. Comparing our results with that of Majaess et al. (2012), we find that 41 (∼ 77%) of the sources classified as YSOs by Majaess et al. (2012), are filtered out as spurious sources on using the stringent and improved source reliability approach proposed by Koenig & Leisawitz (2014).

4 DISCUSSION

4.1 Signatures of cloud-cloud collision

The observed CO morphology and kinematics suggest a cloud-cloud collision scenario for G133.50+9.01 with two distinct cloud components, G133a and G133b. We analyse this complex along the lines discussed in Gong et al. (2017) for the dark cloud L1188. Before we discuss the distinct observational features seen, it is crucial to examine the possibility of the two cloud components being gravitationally bound. The virial mass of the cloud complex can be estimated using the expression (Pillai et al. 2011),

$$M_{\rm vir} = \frac{5\,\sigma^2\,R}{G} \tag{8}$$

where, R is the effective radius of the cloud and $\sigma(= \Delta V/\sqrt{8\ln 2})$ is the velocity dispersion. Both these parameters are obtained using the ^{13}CO (1 − 0) line. R is taken to be equal to $(A/\pi)^{0.5}$, where A is the area considered to derive the total cloud mass and is estimated to be ∼ 2.1 pc. Fitting a Gaussian profile to the ^{13}CO (1−0) spectrum of the entire cloud, we get the line width, ΔV to be 3.5 km s^{-1}. Similar line width is obtained for the spectrum of the intersection region. Taking this, the velocity dispersion is calculated to be 1.5 km s^{-1}. Using these values, we compute the virial mass to be $5.8 \times 10^3\ M_\odot$, which is more than twice the total mass of the cloud complex, $2.6 \times 10^3\ M_\odot$. Within the uncertainties involved in the mass estimations, it is seen that the total mass of the G133.50+9.01 cloud complex is not large enough to be able to gravitationally bind the two clouds. This suggests that the physical association of G133a and G133b with each other must be an accidental event.

In recent years, numerical hydrodynamical simulations and observational studies (e.g. Takahira et al. 2014; Torii et al. 2017; Fukui et al. 2018) have shed light on the various characteristic signatures of cloud-cloud collision. As is evident in Fig. 2, the two clouds, G133a and G133b, are separated by a velocity difference of ∼ 2.8 km s^{-1}. This separation provides a lower limit to the relative collision velocity. The actual collision velocity might be higher than this because of the projection effect (Fukui et al. 2015). As propounded by Inoue & Fukui (2013) and Fukui et al. (2015), the isotropic turbulence is enhanced at the collision-shocked layer, irrespective of the direction of collision. Hence, the velocity spread at the shocked layer can be taken to be similar as the relative collision velocity. Following this, we assume the relative velocity to be the FWHM of the ^{12}CO (1 − 0) line extracted over the intermediate velocity range (−16.9 to −14.1 km s^{-1}) that corresponds to the shock-compressed layer. The FWHM of this line is found to be 5.0 km s^{-1}. Comparing with the velocity difference between the two clouds, the

relative collision velocity translates to a relative motion of the two clouds of ∼ 56° with respect to the line-of-sight.

Another pronounced observational signature of cloud-cloud collision is the "bridging features" detected in the PV diagram. Haworth et al. (2015a,b) made synthetic ^{12}CO PV diagrams using the cloud-cloud collision model data simulated by Takahira et al. (2014). From these observations it was found that the shocked layer is characterised by broad intermediate velocity features, that bridge the colliding clouds in the velocity space. The bridging features often appear at the spots of collision. Several recent studies have provided observational confirmation of such features in the colliding cloud complexes (e.g. Fukui et al. 2016; Torii et al. 2017; Gong et al. 2017). On examining the PV diagram of G133.50+9.01 along the two identified directions A and B as depicted in Fig. 5, we find at least four bridging features clearly visible in the ^{12}CO (1 – 0) and ^{13}CO (1 – 0) emission in the intermediate velocity range of −16.9 to −14.1 km s^{-1}. The green circles in Fig. 5(a) indicate the positions where the bridges appear along the PV cuts. These positions correspond to the spots of collision of the two clouds consistent with the discussions in Fukui et al. (2018). The presence of these bridging features suggests the existence of turbulent gas in the shocked layer that is excited by the collision of the clouds. In addition, the velocity structure in G133.50+9.01 further reveals three high-velocity ^{12}CO (1 – 0) wings, W1, W2 and W3. The locations of these identified wings along the PV cuts are shown in Fig. 5(a). As discussed by Gong et al. (2017, 2019), these high-velocity wings could stem from the outflow(s) driven by one or more YSOs or protostellar cores that have been identified in the intersection region (see Section 4.2).

We examine the cloud at −10 km s^{-1} in the plotted PV diagrams. This cloud displays a rather diffuse morphology in the PV diagrams and is well separated from G133a and G133b. Along the cut B shown in Fig. 5c, an apparent connecting feature is seen but does not resemble a typical 'bridging' structure expected in collision events. Thus, in all likelihood this cloud could well be in the foreground and not physically associated with the G133.50+9.01 complex.

The morphology of the G133.50+9.01 cloud complex as seen in Figs. 2(a)-(c) and 5(a), unveils the picture of an elongated and smaller cloud, G133a, likely in collision with the larger cloud, G133b which displays a 'boomerang-like' structure with a cavity opening in the north-east direction. This is in concordance with simulations done by Anathpindika (2010), Habe & Ohta (1992), Takahira et al. (2014) and Torii et al. (2017). These authors show that when two clouds of different sizes collide, the smaller cloud creates a cavity on the surface of the larger cloud. Evidence supporting this picture was first perceived in the Galactic H II region, RCW 120 (Torii et al. 2015). Here, the observed infrared bubble (or ring) morphology is well explained by cavity creation due to cloud-cloud collision rather than attributing the same to the conventional expansion of HII region scenario for the bubble origin.

4.2 Induced filament, core and cluster formation

As discussed in Section 3.4, distinct filaments are identified which are located in the intersection region of clouds G133a and G133b. As seen in Figs. 6 and 9(b), the filaments detected in G133.50+9.01 present a hub-filament structure. Filament formation is generally understood from the hierarchical collapse of molecular clouds (Motte et al. 2018, and references therein). Following the Hydrodynamic simulations by Habe & Ohta (1992) and Anathpindika (2010), it is seen that the sites of cloud-cloud collision are characterised by a shock compressed layer due to a bow-shock driven by the smaller cloud into the larger cloud. This augurs well with alternate hypothesis for filament formation that has been presented by Inoue & Fukui (2013) and Inoue et al. (2018). Based on their numerical studies using isothermal MHD simulations, these authors conclude that the collision of inhomogeneous clouds lead to the formation of dense filaments in the shock compressed layer, where the magnetic field is amplified in the direction perpendicular to the filament. The clouds are compressed multi-dimensionally except in the direction perpendicular to the background magnetic field, which results in filamentary structures.

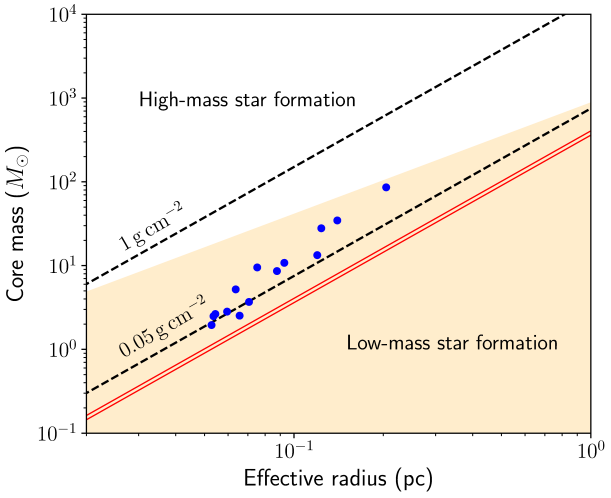


Figure 8. The mass of the dense cores, M_C, identified from the 850 μm map of G133.50+9.01 is plotted as a function of effective radii, r and depicted by blue circles. The red lines indicate the surface density thresholds of 116 $M_\odot$ pc^{-2}(∼ 0.024 g cm^{-2}) and 129 $M_\odot$ pc^{-2}(∼ 0.027 g cm^{-2}) for active star formation from Lada et al. (2010) and Heiderman et al. (2010), respectively. The shaded region delineates the low-mass star forming region that do not satisfy the criterion $m(r) > 870\,M_\odot(r/\mathrm{pc})^{1.33}$ (Kauffmann et al. 2010). The black dashed lines represent the surface density threshold of 0.05 and 1 g cm^{-2} defined by Urquhart et al. (2014) and Krumholz & McKee (2008), respectively.

In the case of G133.50+9.01, the shock compressed layer created at the interacting front manifests as an open arc structure in the ^{12}CO (1 – 0) and ^{13}CO (1 – 0) maps in the intermediate velocity range, −16.9 to −14.1 km s^{-1} as is seen in Fig. 2(b). This arc has a high excitation temperature (13 – 20 K), compared to the ambient medium and an enhanced H_2 column density, evident from Fig. 4. The increase in the H_2 column density within the arc can be due to the multi-dimensional compression of the shocked layer. The filaments detected in the 850 μm map of G133.50+9.01 follows the same orientation of the arc structure. The direction of the magnetic field in the region associated with G133.50+9.01 is determined in Section 3.5, and is sketched in Fig. 6. Concurrent with the results from the MHD simulation by Inoue & Fukui (2013), the background magnetic field, probed using *Planck* data, is seen to be oriented perpendicular to the filamentary structure. It should be noted that the arc could also be the result of stellar feedback (radiation pressure, expanding HII region, outflows from YSOs). From our literature survey, we find no HII region associated with G133.50+9.01, however given the YSOs detected, one cannot conclusively rule out stellar feedback.

Collision induced enhanced density in the intersection region triggers formation of dense cores that accrete matter from the natal filaments. We have detected 14 dust cores in G133.50+9.01, the masses

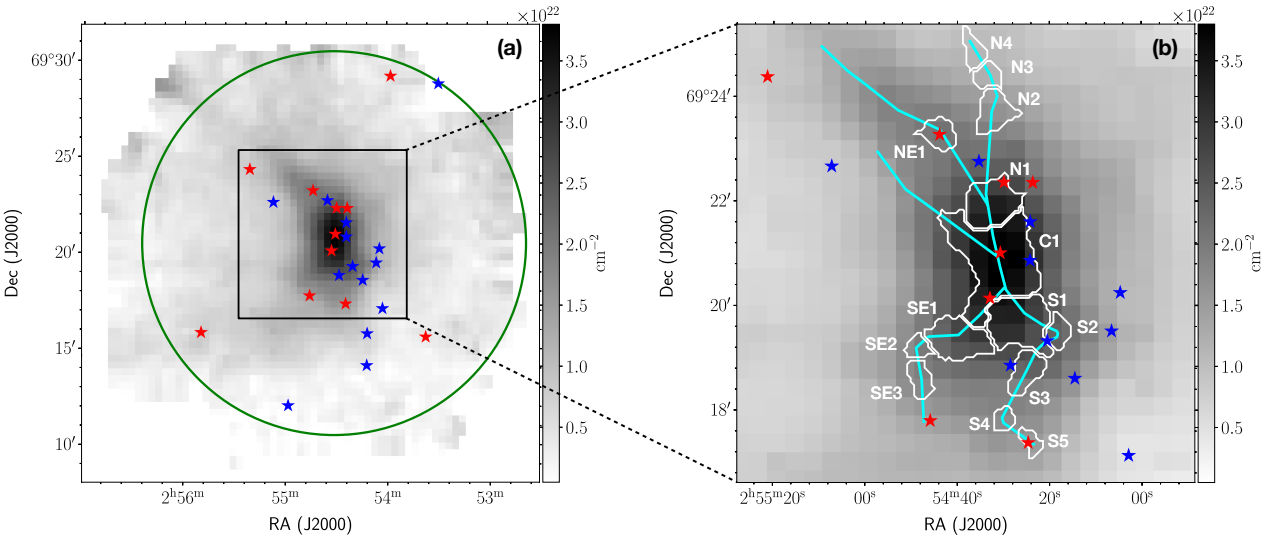


Figure 9. (a) The H_2 column density map same as in Fig. 4(b). The green circle indicates the region over which the YSOs are identified. (b) A zoom-in on the arc which has an enhanced column density. The Class I and Class II YSOs identified, as discussed in Section 3.6, are marked by red and blue stars, respectively. The apertures of the 850 μm dense cores and the skeletons of the filaments are overlaid on (b).

of which are estimated and found to lie within $\sim 2-86\,M_\odot$ with sizes ranging between $\sim 0.05-0.2$ pc. In comparison, Zhang et al. (2018) detect 18 dust cores from the 850 μm continuum map. They use the GaussClumps algorithm for core identification, where only the cores with peak intensities above 5σ are considered. Correlating the dust cores identified by these authors with the ones we extracted using the FellWalker algorithm, we find that majority of the core peaks match. Further, the central core, C1, detected by us encompasses five core peaks identified by Zhang et al. (2018).

In Fig. 8, which is adapted from Yuan et al. (2017) and Liu et al. (2020), we correlate the mass and effective radius of the clumps and interpret their nature. As is discernible from the figure, the dust cores associated with G133.50+9.01 lie comfortably above the mass surface density threshold for active star formation proposed by Lada et al. (2010) and Heiderman et al. (2010). Probing the mass regime possible, we examine the empirical relation, $m(r) > 870 M_\odot (r/\mathrm{pc})^{1.33}$, given by Kauffmann et al. (2010) for high-mass star forming cores. From the estimated mass and radius, the cores associated with G133.50+9.01 do not qualify this threshold and hence should be devoid of high-mass stars. This is somewhat contrary with regards to the limit of 0.05 g cm^{-2} on surface density set by Urquhart et al. (2014) for massive star formation. Barring one, all the active star-forming cores are above this threshold. Hence, it is likely that the more massive cores in our sample are potential high-mass star-forming regions.

We also probe the star-formation activity associated with G133.50+9.01 by inspecting the distribution of the identified YSOs in the region. In Fig. 9(a), we show the YSOs overlaid on the column density map. Of the 25 YSOs detected, a distinct cluster of 18 YSOs is seen to be located in the intersection region. Fig. 9(b) shows an enlarged view with the detected filaments and cores overlaid. From the relative collision velocity of the clouds which is estimated to be 5.0 km s^{-1}, we compute the timescale of collision between G133a and G133b. The ratio of the cloud size, 4.2 pc, to the relative collision velocity gives a collision timescale of ~ 0.8 Myr. It should however be noted that this gives an order-of-magnitude estimate, at best. The value might vary by a factor of ~ 2 owing to projection effects in space and velocity and to the unknown configuration of the clouds before collision (Fukui et al. 2014). Nonetheless, the timescale derived is longer than the typical lifetimes of Class I YSOs and is comparable to the lifetime of Class II YSOs. As discussed in Dunham et al. (2015) and Evans et al. (2009), the age estimates of Class I and Class II YSOs are 0.4-0.7 Myr and 2 ± 1 Myr, respectively. The scenario that has unfolded in G133.50+9.01 gives compelling evidence of this being a bona fide case of collision induced cluster formation. Similar results are obtained in several other studies focused towards cloud collision and induced cluster formation (e.g. Torii et al. 2011; Gong et al. 2017).

5 CONCLUSIONS

Gas kinematics studied using the CO lines show a picture of colliding clouds G133a and G133b triggering the formation of a complex network of filaments, dense cores and YSOs in G133.50+9.01 complex. Fig. 10 depicts a schematic of the chain of events occurring. Clouds G133a and G133b with a velocity difference of ~ 2.8 km s^{-1} are likely to have collided forming a shock-compressed layer in the intersection region. Conforming to MHD simulations, the formation of a complex network of filaments is deduced from the 850 μm map. 14 dust cores that accrete matter from the natal filaments are also identified. The over-density of Class I and II YSOs along the intersection arc advocates for collision induced cluster formation in G133.50+9.01. Keeping in mind that the PMO observations presented in this paper might not have sampled the entire complex, an accurate interpretation of the morphology of the colliding clouds is difficult. Further, the resolution of the data used is not adequate to correlate the observed scenario with either the spherical cloud collision models (e.g. Habe & Ohta 1992; Takahira et al. 2014) or filamentary cloud collision simulations (Li et al. 2018). Nonetheless, observational features seen makes G133.50+9.01 an interesting candidate to probe cloud-cloud collision. With follow-up high-resolution molecular line and dust continuum observations, viable models can be explored to explain the observed signatures.

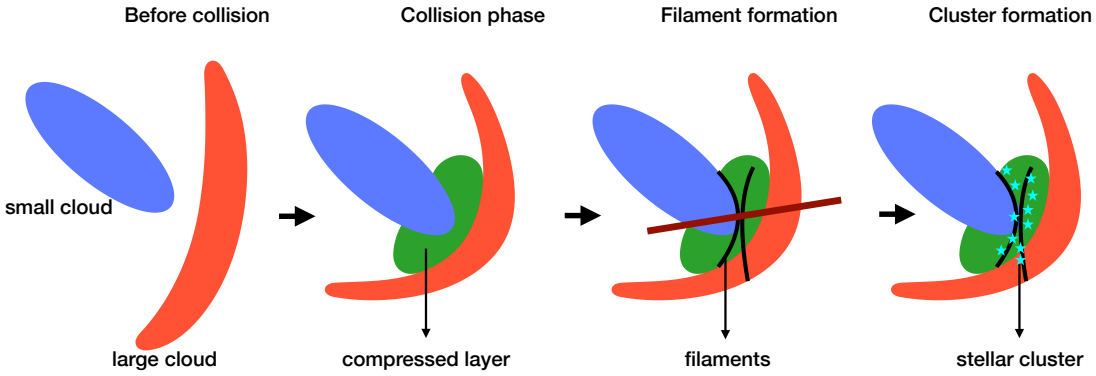


Figure 10. A schematic of the cloud-cloud collision in G133.50+9.01 depicting the scheme of events from the time of collision of G133a (small cloud) with G133b (large cloud). The orientation of the background magnetic field is indicated by the maroon line.

ACKNOWLEDGEMENTS

We would like to thank the referee for valuable comments/suggestions. The authors would like to thank Dr. Pak Shing Li for fruitful discussions. We are grateful to the staff at the Qinghai Station of PMO for their assistance during the observations. The James Clerk Maxwell Telescope is operated by the East Asian Observatory on behalf of The National Astronomical Observatory of Japan; Academia Sinica Institute of Astronomy and Astrophysics; the Korea Astronomy and Space Science Institute; Center for Astronomical Mega-Science (as well as the National Key R&D Program of China with No. 2017YFA0402700). Additional funding support is provided by the Science and Technology Facilities Council of the United Kingdom and participating universities in the United Kingdom and Canada. Additional funds for the construction of SCUBA-2 were provided by the Canada Foundation for Innovation. This publication makes use of data products from the *Wide-field Infrared Survey Explorer*, which is a joint project of the University of California, Los Angeles, and the Jet Propulsion Laboratory/California Institute of Technology, funded by the National Aeronautics and Space Administration.

DATA AVAILABILITY

The original data underlying this article will be shared on reasonable request to the corresponding author.

REFERENCES

Anathpindika S. V., 2010, MNRAS, 405, 1431
Berry D., 2015, Astronomy and Computing, 10, 22
Corradi R. L. M., Aznar R., Mampaso A., 1998, MNRAS, 297, 617
Cutri R. M., et al. 2013, VizieR Online Data Catalog, p. II/328
Dunham M. M., et al., 2015, ApJS, 220, 11
Evans Neal J. I., et al., 2009, ApJS, 181, 321
Frerking M. A., Langer W. D., Wilson R. W., 1982, ApJ, 262, 590
Fukui Y., et al., 2014, ApJ, 780, 36
Fukui Y., et al., 2015, ApJ, 807, L4
Fukui Y., et al., 2016, ApJ, 820, 26
Fukui Y., et al., 2018, ApJ, 859, 166
Fukui Y., Habe A., Inoue T., Enokiya R., Tachihara K., 2020, arXiv e-prints, p. arXiv:2009.05077
Gong Y., et al., 2017, ApJ, 835, L14
Gong Y., et al., 2019, A&A, 632, A115
Green G. M., Schlafly E., Zucker C., Speagle J. S., Finkbeiner D., 2019, ApJ, 887, 93
Habe A., Ohta K., 1992, PASJ, 44, 203
Haworth T. J., et al., 2015a, MNRAS, 450, 10
Haworth T. J., Shima K., Tasker E. J., Fukui Y., Torii K., Dale J. E., Takahira K., Habe A., 2015b, MNRAS, 454, 1634
Hayashi K., et al., 2020, Triggered high-mass star formation in the HII region W28A2: A cloud-cloud collision scenario (arXiv:2005.07933)
Heiderman A., Evans Neal J. I., Allen L. E., Huard T., Heyer M., 2010, ApJ, 723, 1019
Holland W. S., et al., 2013, MNRAS, 430, 2513
Inoue T., Fukui Y., 2013, ApJ, 774, L31
Inoue T., Hennebelle P., Fukui Y., Matsumoto T., Iwasaki K., Inutsuka S.-i., 2018, PASJ, 70, S53
Kauffmann J., Pillai T., Shetty R., Myers P. C., Goodman A. A., 2010, ApJ, 716, 433
Koenig X. P., Leisawitz D. T., 2014, ApJ, 791, 131
Krumholz M. R., McKee C. F., 2008, Nature, 451, 1082
Lada C. J., Lombardi M., Alves J. F., 2010, ApJ, 724, 687
Li P. S., Klein R. I., McKee C. F., 2018, MNRAS, 473, 4220
Liu T., Wu Y., Zhang H., 2012, ApJS, 202, 4
Liu T., et al., 2018a, ApJS, 234, 28
Liu T., et al., 2018b, ApJ, 859, 151
Liu T., et al., 2020, MNRAS, 496, 2790
Mainzer A., et al., 2011, ApJ, 731, 53
Majaess D., Turner D. G., Gieren W., 2012, MNRAS, 421, 1040
Motte F., Bontemps S., Louvet F., 2018, ARA&A, 56, 41
Ohama A., et al., 2018, PASJ, 70, S45
Pillai T., Kauffmann J., Wyrowski F., Hatchell J., Gibb A. G., Thompson M. A., 2011, A&A, 530, A118
Planck Collaboration et al., 2015, A&A, 576, A104
Planck Collaboration et al., 2016a, A&A, 594, A1
Planck Collaboration et al., 2016b, A&A, 594, A26
Reid M. J., Dame T. M., Menten K. M., Brunthaler A., 2016, ApJ, 823, 77
Sano H., et al., 2018, PASJ, 70, S43
Sano H., et al., 2019, arXiv e-prints, p. arXiv:1908.08404
Shan W., et al., 2012, IEEE Transactions on Terahertz Science and Technology, 2, 593
Szűcs L., Glover S. C. O., Klessen R. S., 2016, MNRAS, 460, 82
Takahira K., Tasker E. J., Habe A., 2014, ApJ, 792, 63

Tasker E. J., Tan J. C., 2009, ApJ, 700, 358
Tokuda K., et al., 2019, ApJ, 886, 15
Torii K., et al., 2011, ApJ, 738, 46
Torii K., et al., 2015, ApJ, 806, 7
Torii K., et al., 2017, ApJ, 835, 142
Urquhart J. S., et al., 2014, MNRAS, 443, 1555
Wilson T. L., Rood R., 1994, ARA&A, 32, 191
Wright E. L., et al., 2010, AJ, 140, 1868
Wu Y., Liu T., Meng F., Li D., Qin S.-L., Ju B.-G., 2012, ApJ, 756, 76
Wu B., Van Loo S., Tan J. C., Bruderer S., 2015, ApJ, 811, 56
Yuan J., et al., 2017, ApJS, 231, 11
Zhang C.-P., et al., 2018, ApJS, 236, 49

This paper has been typeset from a TEX/LATEX file prepared by the author.